Unidirectional Emission of a Quantum Dot Coupled to a Nanoantenna

Alberto G. Curto, *et al.*

Science **329**, 930 (2010);
DOI: 10.1126/science.1191922

18. C. Palenzuela, L. Lehner, S. Yoshida, *Phys. Rev. D* **81**, 084007 (2010).
19. P. Mösta *et al.*, *Phys. Rev. D* **81**, 064017 (2010).
20. See supporting material on *Science* Online.
21. P. Goldreich, W. H. Julian, *Astrophys. J.* **157**, 869 (1969).
22. S. S. Komissarov, *Mon. Not. R. Astron. Soc.* **350**, 427 (2004).
23. V. Semenov, S. Dyadechkin, B. Punsly, *Science* **305**, 978 (2004).
24. S. S. Komissarov, J. C. McKinney, *Mon. Not. R. Astron. Soc. Lett.* **377**, L49 (2007).
25. A. Tchekhovskoy, J. C. McKinney, R. Narayan, *Mon. Not. R. Astron. Soc.* **388**, 551 (2008).
26. J. H. Krolik, J. Hawley, in *The Jet Paradigm: From Microquasars to Quasars*, vol. 794 of *Lecture Notes in Physics* (Springer, Berlin, 2010), pp. 265–287.
27. M. Vietri, *Astrophys. J.* **471**, L95 (1996).
28. R. R. Rafikov, P. Goldreich, *Astrophys. J.* **631**, 488 (2005).
29. R. A. Matzner *et al.*, *Science* **270**, 941 (1995).
30. C. D. Dermer, J. D. Finke, G. Menon, http://arxiv.org/abs/0810.1055 (2008).
31. P. Mösta *et al.*, *Phys. Rev. D* **81**, 064017 (2010).
32. A. Vecchio, *Phys. Rev. D* **70**, 042001 (2004).

33. We thank A. Broderick, N. Afshordi, T. Garrett, R. MacNamara, E. Poisson, A. Spitkovsky, and C. Thompson, as well as our longtime collaborators D. Neilsen, E. Hirschmann, P. Motl, and M. Anderson, for useful discussions and comments. Supported by NSF grants PHY-0803629 (to Louisiana State University) and PHY-0803624 (to Long Island University) and by a Natural Sciences and Engineering Research Council of Canada Discovery Grant. Research at Perimeter Institute is supported through Industry Canada and by the Province of Ontario through the Ministry of Research and Innovation. The computations were performed in Teragrid and Scinet. C.P. and L.L. thank the Princeton Center for Theoretical Physics, where parts of this work were completed, for its hospitality.

Supporting Online Material

www.sciencemag.org/cgi/content/full/329/5994/927/DC1
Materials and Methods
Fig. S1
Movies S1 and S2
References

3 May 2010; accepted 7 July 2010
10.1126/science.1191766

Unidirectional Emission of a Quantum Dot Coupled to a Nanoantenna

Alberto G. Curto,[1] Giorgio Volpe,[1] Tim H. Taminiau,[1] Mark P. Kreuzer,[1] Romain Quidant,[1,2] Niek F. van Hulst[1,2]*

Nanoscale quantum emitters are key elements in quantum optics and sensing. However, efficient optical excitation and detection of such emitters involves large solid angles because their interaction with freely propagating light is omnidirectional. Here, we present unidirectional emission of a single emitter by coupling to a nanofabricated Yagi-Uda antenna. A quantum dot is placed in the near field of the antenna so that it drives the resonant feed element of the antenna. The resulting quantum-dot luminescence is strongly polarized and highly directed into a narrow forward angular cone. The directionality of the quantum dot can be controlled by tuning the antenna dimensions. Our results show the potential of optical antennas to communicate energy to, from, and between nano-emitters.

Optical antennas, acting as converters between propagating and localized fields, provide an effective route to couple photons in and out of nanoscale objects. These antennas are the counterparts of conventional radio and microwave antennas and operate in the visible regime (*1*, *2*). Optical antennas have been shown to focus optical fields to subdiffraction-limited volumes (*3*), enhance the excitation and emission of quantum emitters (*4*–*7*), and modify their spectra (*8*).

A characteristic of antennas is their directed emission and reception. So far, the control of directionality has mainly been pursued by photonic crystal structures (*9*) and surface-plasmon–based devices (*10*–*12*). However, for such structures approaching the nanometer scale diffraction can limit the collimated beaming of light. On the other hand, the interaction of quantum emitters with light is best enhanced with microcavities (*13*, *14*). Compared with these approaches, plasmonic nanoantennas offer a much smaller footprint in an open geometry combining strong subwavelength fields and increased transition rates, together with the prospect of directionality.

Earlier work (*15*–*17*) observed variations in the angular emission of molecules by the presence of metallic objects in their near field. From experience at radio and microwave frequencies, it is known that highly directed beams are commonly obtained with Yagi-Uda antennas (*18*). In the optical regime, directional far-field scattering of a polarized laser beam from an array of Yagi-Uda antennas has been recently presented (*19*). Complete control of the direction of light emission from a single quantum emitter using an optical Yagi-Uda antenna has been theoretically proposed (*20*–*22*).

We report the realization and observation of unidirectional nanoscale photon sources by coupling single-quantum systems to a Yagi-Uda design. The realization of such a source requires the precise near-field coupling of an emitter to a nanoscale antenna that is tuned to the emission spectrum. To this end, a quantum dot (QD) is placed at the resonant feed element of a nanofabricated Yagi-Uda antenna.

A Yagi-Uda antenna consists of an actively driven feed element surrounded by a set of parasitic elements acting as reflectors and directors (Fig. 1A). The reflectors and directors are de-

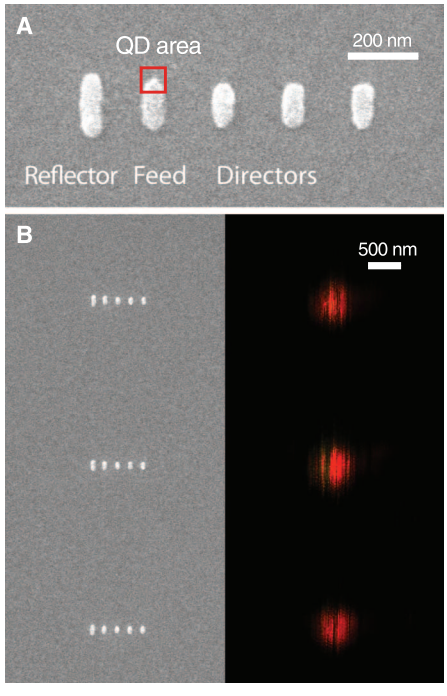

Fig. 1. Optical Yagi-Uda antennas driven by quantum dots. (**A**) Scanning electron microscopy (SEM) image of fabricated five-element Yagi-Uda antenna consisting of a feed element, one reflector, and three directors (YU145). A QD is attached to one end of the feed element inside the marked area. (**B**) Comparison of SEM and scanning confocal luminescence microscopy images of three antennas driven by QDs. The image is color-coded for degree of linear polarization [(C), inset]. (**C**) Intensity time trace of luminescence in both polarization channels for one of the antennas in (B), showing blinking of a single QD.

[1]Institut de Ciencies Fotoniques (ICFO), Mediterranean Technology Park, 08860 Castelldefels (Barcelona), Spain. [2]Institució Catalana de Recerca i Estudis Avançats (ICREA), 08015 Barcelona, Spain.

*To whom correspondence should be addressed. E-mail: niek.vanhulst@icfo.es

tuned in length with respect to the dipolar resonance of the feed, and the spacing between elements is chosen so that a traveling wave pointing toward the directors is created. Numerical simulations were used to design five-element gold Yagi-Uda antennas for operation wavelengths of ~800 nm (*23*).

To obtain a strong near-field coupling of a QD to the antenna mode, it is critical to place the emitter at a position of high electric mode density—that is, at one of the ends of the feed element. We used a two-step electron beam lithography process combined with chemical functionalization (*23*). The first lithography step defined the antenna structures on a glass substrate, followed by thermal evaporation of a 30-nm layer of gold. The second lithography step set the boundaries for the formation of a self-assembled monolayer of mercaptoundecanoic acid exclusively on the predefined exposed areas. Core-shell QDs were immobilized on the functionalized areas (70-nm squares), and the remaining resist was removed. A typical fabricated antenna is shown (Fig. 1A) with feed length L_f = 145 nm, spacing a_r = 175 nm between reflector and feed, and spacing a_d = 200 nm between directors. The total length is 830 nm, which is approximately one emission wavelength.

The emission of QDs on antennas was characterized with a confocal microscope with three dedicated detection branches: for luminescence imaging, angular detection, and spectroscopy, respectively (*23*). The use of a high–numerical aperture (NA) objective (1.46 NA) is essential for the angular detection. The sample is excited by a circularly polarized He-Ne laser beam [wavelength (λ) = 633 nm], which is focused to address a single antenna at a time. The resulting luminescence is separated from the excitation wavelength with a dichroic mirror and a long-pass filter. For confocal detection, the use of a polarizing beam-splitter and two detection channels ($I_\parallel$ and $I_\perp$) with avalanche photodiodes allows us to determine polarization anisotropies. For detection of the angular emission, we recorded images of the intensity distribution on the back focal plane of the high-NA objective (conoscopy) (*24*) on an electron-multiplying charge-coupled device (emCCD) camera. These Fourier-plane images (momentum space) contain the directions of emission toward the substrate.

All presented confocal luminescence images are color-coded (red-yellow-green) for the degree of linear polarization (DOLP) [DOLP = $(I_\parallel - I_\perp)/(I_\parallel + I_\perp)$], with red being linear polarization parallel to the feed longitudinal axis. All antenna-QD systems in Fig. 1B show red (linearly polarized), confirming that the QD drives the linear dipole of the feed element (*15*, *25*). The QDs are cleanly positioned on the antennas, and the emission arises from quantum emitters as discrete blinking events interrupt the signal during raster-scanning of the sample. This blinking is better seen in the luminescence time trace displayed in Fig. 1C, in which clear on and off states can be identified, which is characteristic of a single emitter. From many such time traces, we conclude that single QDs occur frequently, whereas the typical number of QDs observed is one, two, or three—a number that can be controlled by both the size of the functionalized area and the concentration of the deposited QD solution.

To gain direct insight into the changes in the QD emission upon coupling to the antenna, we compared three types of nanostructures (Fig. 2, A and B): small 60-nm gold squares, λ/2 dipole antennas, and the Yagi-Uda antennas. The small, off-resonant squares were taken as a reference for QDs on metal; the dipole antennas are essentially the feed element of a Yagi-Uda antenna. In the reference case, the polarization of the luminescence varies, with a DOLP ranging from –0.5 to 0.5 (Fig. 2A, first column) because the QDs have different orientations and the gold squares induce no preferential direction. The corresponding emission pattern is shown in Fig. 2B. The momentum space images contain two distinct circles in the polar angle θ: The outer circle is the maximum collection angle of our objective (θ_{NA} = 72.8°), whereas the inner circle is the critical angle for the glass-air interface (θ_c = 41.1°). A dipole close to an interface emits primarily into the high-index medium, with sharply peaked maxima at the critical angle. Moreover, our QDs exhibit a degenerate transition dipole moment contained on a "bright" plane (*26*, *27*). As a result, the radiation pattern of a QD is nearly isotropic in the azimuthal angle φ.

When coupled to a λ/2 dipole resonant nanoantenna (Fig. 2, second column), the picture changes dramatically: The QD luminescence turns into a clear linear polarization parallel to the long axis of the antenna (DOLP ≈ 0.8), and the radiation pattern transforms to that of a linear dipole close to an interface (*24*). These are two clear signatures of the near-field coupling (*15*). The QD emission becomes fully determined by the antenna mode, both in polarization and direction, despite the degeneracy of the QD dipole moment.

We can also control the emission direction by positioning the QDs at one end of the λ/2 feed element of Yagi-Uda antennas (Fig. 2, third column). The luminescence remains strongly linearly polarized (DOLP ≈ 0.8), but the radiation pattern now shows a single lobe, demonstrating the unidirectional emission of a QD due to coupling to an optical antenna.

The directional performance can be quantified by a front-to-back ratio (*F*/*B*), defined as the intensity ratio between the point with maximum

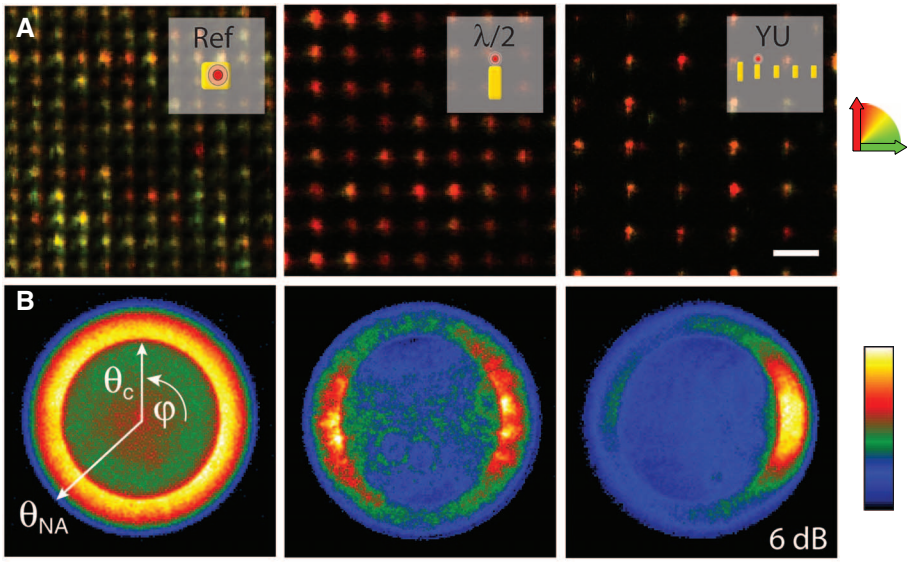

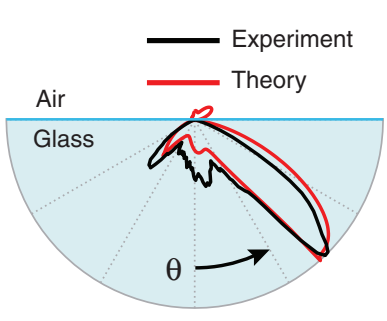

Fig. 2. Unidirectional emission of a QD coupled to an optical Yagi-Uda antenna and comparison with other metal nanostructures. (**A**) Scanning confocal luminescence images of QDs on reference 60-nm gold squares (Ref), half-wave dipole antennas (λ/2), and Yagi-Uda antennas (YU), respectively. Different colors show variations in degree of linear polarization. YU corresponds to antennas, with the parameter set YU145. The schematics in the insets are not to scale. Scale bar, 2 μm. (**B**) Radiation pattern (intensity distribution at the back focal plane of the objective) from an individual structure in (A). Critical (θ_C) and numerical aperture (θ_{NA}) angles are indicated. For YU, a 830-nm long-pass filter was used. (**C**) Angular radiation pattern in the polar angle (θ) for the Yagi-Uda antenna (black), which is in good agreement with the theoretical prediction (red).

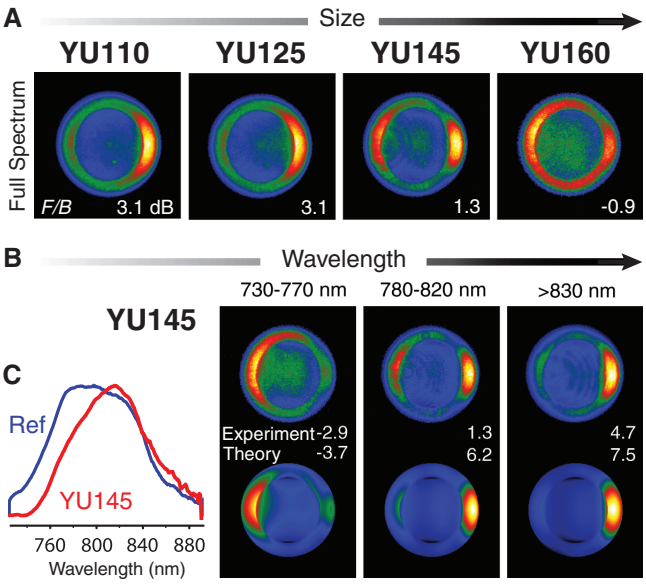

Fig. 3. Tuning of optical Yagi-Uda antennas. (**A**) Radiation patterns in the back focal plane of the objective for four different individual Yagi-Uda antennas of increasing overall size, characterized by the length of the feed element L_f from 110 to 160 nm. The full emission spectrum was recorded. (**B**) Angular radiation patterns for different spectral detection windows for the YU145 shown in (A). Theory and experiment are compared. The front-to-back ratio in decibels is indicated for each pattern. (**C**) Luminescence spectra of QDs coupled to the reference and YU145.

emitted power and the point diametrically opposite in the radiation pattern. The *F*/*B* value is essentially 0 dB for the reference squares and the dipole antennas, as expected for symmetrical structures. For the Yagi-Uda antenna in Fig. 2B, *F*/*B* is 6.0 dB. The directed emission is centered at $\theta = 49.4°$, with a beam half width at half maximum of 12.5° in θ and 37.0° in φ. The experimental angular radiation pattern can be calculated from the Fourier-plane image (*23*) and agrees well with the theoretical prediction (Fig. 2D). The simulations quantify that as much as 83.2% of the QD emission is directed into the high-index glass substrate. The emission is thus truly unidirectional, unlike configurations with a low-index contrast interface, which results in two separate emission lobes (*19*). The total brightness of the QDs coupled to Yagi-Uda antennas is comparable with that of dipole antennas. This observation is in agreement with our calculations and previous theoretical predictions (*21*), which show that adding the parasitic antenna elements does not strongly reduce the antenna radiation efficiency (only a 10 to 20% reduction). The Yagi-Uda antenna redirects the emission instead of suppressing one half of the radiation. Because of excitation enhancement, the number of counts detected from both types of antennas is much higher than for a QD on glass without coupling to an antenna.

Any Yagi-Uda antenna is designed to operate at a certain frequency and bandwidth. To assess the frequency dependence of the directionality, we fabricated Yagi-Uda antennas tuned to four different resonant frequencies (Fig. 3A), identified with their feed element lengths L_f: 110 to 160 nm (a complete parameter can be found in table S1). Increasing the antenna length creates a redshift of the resonance. The shortest antennas (YU110 and YU125) emit clearly unidirectionally. These antennas are tuned close to the QD emission, and their bandwidth contains the complete luminescence spectrum. These observations are in agreement with a calculated bandwidth of 150 nm for end-fire operation, defined as $F/B > 3$ dB. On the other hand, for longer antennas (YU145 and YU160) the antenna resonance is more detuned from the QD emission, and directivity is hindered by short-wavelength components of the spectrum. This spectral dependence does also occur for radio frequency Yagi-Uda antennas (*28*) and was in fact predicted for the optical regime (*20*, *29*).

To corroborate the analysis above, we evaluated the dependence of the directionality on the wavelength of the emitted photons for a given antenna, YU145 (Fig. 3, B and C). This antenna was red-detuned from the QD emission. As a result, the QD emission spectrum was modified by the near-field coupling to the antenna (Fig. 3C) (*8*). The emission spectrum of an individual YU145 antenna was divided in three parts by using three different filters. Although hardly any directed emission was observed for the complete spectrum (Fig. 3A), a high directivity was recovered when only the long-wavelength part of the spectrum was selected (Fig. 3B). For short wavelengths—below a cut-off value—the emission was even reversed, with the main lobe pointing backward. Similar behavior was observed for the longer antenna YU160, with all characteristic wavelengths shifted to longer wavelengths. The numerically calculated back-focal-plane images agree well with the experimental results (Fig. 3B). The maximum experimental *F*/*B* values tend to be lower than the theoretical values because part of the signal stems from autoluminescence of the gold nanoparticles and a fraction of the QD emission is not coupled to the antenna, both of which contribute to a minor isotropic background. Thus, by tuning the antenna or selecting certain emission bands the frequency dependence of the directivity of an optical Yagi-Uda antenna is proved.

The presented antenna transforms the non-directional QD luminescence into a directed light source that can be efficiently collected, simply with a low NA. Further optimization of the many Yagi-Uda design parameters, including the addition of more director elements, might sharpen up the unidirectional cone and tune the central emission angle. The operation bandwidth can be increased by the use of a log-periodic design (*2*). By reciprocity, the antennas should work both in emission and absorption. The near-field coupling to the antenna plasmon resonance enhances radiative transition rates, increasing the emission efficiency. All this control over photon emission is obtained from an antenna that is only a single wavelength long. Unidirectional optical antennas thus provide a route to effectively communicate light to, from, and between nano-emitters, for example in directed, bright single-photon sources for quantum optical technologies, planar biochemical sensors, and light-harvesting and emission devices.

References and Notes

1. P. Bharadwaj, B. Deutsch, L. Novotny, *Adv. Opt. Photon.* **1**, 438 (2009).
2. C. A. Balanis, *Antenna Theory: Analysis and Design* (Wiley, New Jersey, ed. 3, 2005).
3. T. H. Taminiau, R. J. Moerland, F. B. Segerink, L. Kuipers, N. F. van Hulst, *Nano Lett.* **7**, 28 (2007).
4. A. Kinkhabwala *et al.*, *Nat. Photonics* **3**, 654 (2009).
5. J. N. Farahani, D. W. Pohl, H. J. Eisler, B. Hecht, *Phys. Rev. Lett.* **95**, 017402 (2005).
6. S. Kühn, U. Håkanson, L. Rogobete, V. Sandoghdar, *Phys. Rev. Lett.* **97**, 017402 (2006).
7. O. L. Muskens, V. Giannini, J. A. Sánchez-Gil, J. Gómez Rivas, *Nano Lett.* **7**, 2871 (2007).
8. M. Ringler *et al.*, *Phys. Rev. Lett.* **100**, 203002 (2008).
9. P. Kramper *et al.*, *Phys. Rev. Lett.* **92**, 113903 (2004).
10. H. J. Lezec *et al.*, *Science* **297**, 820 (2002).
11. N. F. Yu *et al.*, *Nat. Photonics* **2**, 564 (2008).
12. F. López-Tejeira *et al.*, *Nat. Phys.* **3**, 324 (2007).
13. M. Pelton *et al.*, *Phys. Rev. Lett.* **89**, 233602 (2002).
14. A. Badolato *et al.*, *Science* **308**, 1158 (2005).
15. T. H. Taminiau, F. D. Stefani, F. B. Segerink, N. F. van Hulst, *Nat. Photonics* **2**, 234 (2008).
16. H. Gersen *et al.*, *Phys. Rev. Lett.* **85**, 5312 (2000).
17. S. Kühn, G. Mori, M. Agio, V. Sandoghdar, *Mol. Phys.* **106**, 893 (2008).
18. H. Yagi, *Proc. IRE* **16**, 715 (1928).
19. T. Kosako, Y. Kadoya, H. F. Hofmann, *Nat. Photonics* **4**, 312 (2010).
20. H. F. Hofmann, T. Kosako, Y. Kadoya, *N. J. Phys.* **9**, 217 (2007).
21. T. H. Taminiau, F. D. Stefani, N. F. van Hulst, *Opt. Express* **16**, 10858 (2008).
22. J. J. Li, A. Salandrino, N. Engheta, *Phys. Rev. B* **76**, 245403 (2007).
23. Materials and methods are available as supporting material on *Science* Online.
24. M. A. Lieb, J. M. Zavislan, L. Novotny, *J. Opt. Soc. Am. B* **21**, 1210 (2004).
25. T. Shegai *et al.*, *Proc. Natl. Acad. Sci. U.S.A.* **105**, 16448 (2008).
26. F. Koberling *et al.*, *J. Phys. Chem. B* **107**, 7463 (2003).
27. X. Brokmann, L. Coolen, J. P. Hermier, M. Dahan, *Chem. Phys.* **318**, 91 (2005).

28. N. K. Takla, L. C. Shen, *IEEE Trans. Antenn. Propag.* **25**, 913 (1977).
29. A. F. Koenderink, *Nano Lett.* **9**, 4228 (2009).
30. We thank M. Castro-López for help in developing the fabrication method and M. U. González, F. Kulzer, F. D. Stefani, D. Brinks, and R. Hildner for helpful discussions. This research was funded by the Spanish Ministry of Science and Innovation (MICINN) and the Ministry of Education through programs FIS2009-08203, CONSOLIDER CSD2007-046, FPU (A.G.C. and G.V.), FPI (T.H.T.) and Ramón y Cajal (M.P.K.), Fundació CELLEX Barcelona (G.V., M.P.K., R.Q., and N.F.v.H.), and the European Research Council Advanced Grant (N.F.v.H.).

Supporting Online Material
www.sciencemag.org/cgi/content/full/329/5994/930/DC1
Materials and Methods
Table S1

6 May 2010; accepted 12 July 2010
10.1126/science.1191922

Ceria Maintains Smaller Metal Catalyst Particles by Strong Metal-Support Bonding

Jason A. Farmer and Charles T. Campbell*

The energies of silver (Ag) atoms in Ag nanoparticles supported on different cerium and magnesium oxide surfaces, determined from previous calorimetric measurements of metal adsorption energies, were analyzed with respect to particle size. Their stability was found to increase with particle size below 5000 atoms per particle. Silver nanoparticles of any given size below 1000 atoms had much higher stability (30 to 70 kilojoules per mole of silver atoms) on reduced CeO_2(111) than on MgO(100). This effect is the result of the very large adhesion energy (~2.3 joules per square meter) of Ag nanoparticles to reduced CeO_2(111), which we found to be a result of strong bonding to both defects and CeO_2(111) terraces, apparently localized by lattice strain. These results explain the unusual sinter resistance of late transition metal catalysts when supported on ceria.

Nanoparticles of late transition metals adsorbed on oxide surfaces form the basis for many catalysts important in energy technology, pollution prevention, and environmental cleanup. The catalytic activity per surface metal atom and selectivity can depend strongly on the particle size below 6 nm (*1*–*5*), the choice of oxide support (*1*, *2*, *6*–*21*), and the extent of oxide reduction (*22*–*26*). Furthermore, the metal nanoparticles often sinter—they form fewer, larger particles—under catalytic reaction conditions and even during catalyst preparation. Sintering results in loss of activity or selectivity, mainly through a decrease in the number of exposed metal atoms but also through the loss of the smallest particles, which may have electronic properties that make them especially reactive. Late transition metal catalysts have also been reported to sinter more slowly or maintain smaller particles when supported on CeO_2 relative to other supports (*16*, *19*, *21*). To fundamentally understand such structure-reactivity relations in catalytic phenomena, it is important to know how the energy of transition metal atoms in catalyst nanoparticles depends on the particle size and the nature of the oxide support surface to which they bind.

Here, we analyzed our previous calorimetric measurements of the adsorption energies of Ag vapor onto different oxide surfaces, on which Ag nanoparticles grow with very similar size and number density upon adsorption. These data allow for a quantitative comparison of variations of the energy of Ag atoms in Ag nanoparticles of different sizes, We next compared how the stability of a metal particle of a given size depends on the nature of the oxide surface to which it is attached. This analysis provides a quantitative estimate of the underlying thermodynamic reasons why late transition metal catalysts maintain smaller particle sizes and better resist sintering when on ceria supports relative to other oxide materials. By comparing ceria surfaces with different extents of reduction, we could assess qualitatively the stabilizing effect of surface oxygen vacancies on the adhesion energy of Ag nanoparticles to ceria. These results help to explain why ceria often enhances the performance of late transition metal catalysts—especially their unusual sinter resistance relative to other supports—in a wide variety of reactions in energy and environmental technology (*8*, *11*, *13*, *15*–*21*). The results also show that metal-oxide adhesion is locally stronger around oxide defects.

Our calorimetric measurements of the adsorption energies of Ag gas atoms onto clean and ordered surfaces of CeO_{2-x}(111) films (with x = 0.1 and 0.2) are described in detail elsewhere (*27*). The CeO_{2-x}(111) films were grown on Pt(111), and results were compared for film thicknesses of 1, 2, 3, and 4 nm (*27*). The Ce(3d) region in the X-ray photoelectron spectroscopy (XPS) was used to measure the Ce^{3+}/Ce^{4+} concentration ratio within the probe depth of XPS (~1 nm), as described in (*28*), which was found to be 1:4 for the as-grown films. We describe these surfaces as CeO_{2-x}(111), with $x = 0.1$, or as $CeO_{1.9}$(111), which denotes CeO_2(111) with 5% oxygen vacancies (*29*). The total density of steps and kinks was estimated from scanning tunneling microscopy (STM) images and low-energy electron diffraction spot widths to be ~6% of the total surface atoms, and most of the vacancies were probably localized at these step or kink defects (*27*). Measurements of the Ce^{3+}/Ce^{4+} ratio were also performed on such 4-nm films after further thermal reduction by heating in ultrahigh vacuum, for which x was shown to increase to 0.2; we refer to the resulting films as $CeO_{1.8}$(111) (*27*).

The measurements of the heat of adsorption for Ag on MgO(100) films that we analyze here have also been reported previously (*30*). The MgO(100) was 4 nm thick and grown on Mo(100) (*30*), and later proved to have ~5% step and kink sites as

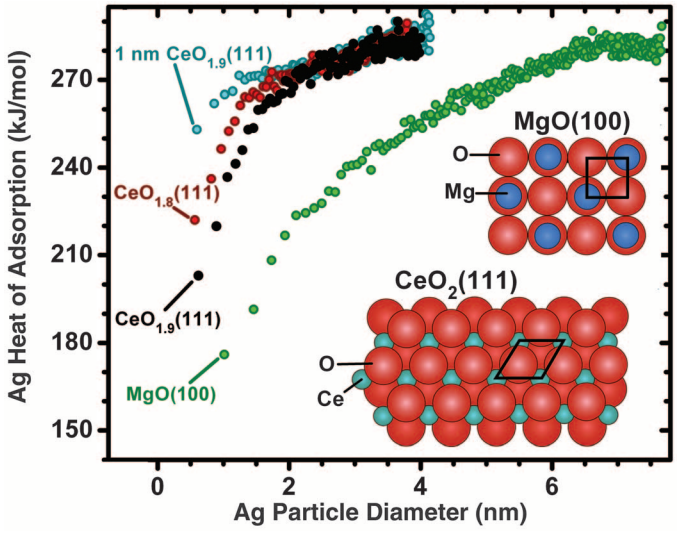

Fig. 1. Measured heat of Ag atom adsorption versus the Ag particle diameter to which it adds, for Ag adsorption onto four different surfaces: two 4-nm CeO_2(111) films with different extents of surface reduction (x = ~0.1 and 0.2 in CeO_{2-x}), grown on Pt(111); a 1-nm $CeO_{1.9}$(111) film grown on Pt(111); and a 4-nm MgO(100) film grown on Mo(100). The inset shows structural models for perfect CeO_2(111) and MgO(100), with their unit cells in black lines.

Department of Chemistry, Box 351700, University of Washington, Seattle, WA 98195, USA.

*To whom correspondence should be addressed. E-mail: campbell@chem.washington.edu